Tomography of Southern California via Bayesian Joint Inversion of Rayleigh Wave Ellipticity and Phase Velocity from Ambient Noise Cross-Correlations

E. M. Berg[1], F.-C. Lin[1], A. Allam[1], H. Qiu[2], W. Shen[3], Y. Ben-Zion[2]

[1]Department of Geology and Geophysics, University of Utah, Salt Lake City, UT, USA

[2]Department of Earth Sciences, University of Southern California, Los Angeles, CA, USA

[3]Department of Geosciences, Stony Brook University, Stony Brook, NY, USA

Corresponding author: Elizabeth Berg (e.m.berg@utah.edu)

Key Points:

- Ambient noise cross-correlations across Southern California show clear Rayleigh waves with measurable phase and amplitude information
- Amplitude information, through Rayleigh ellipticity (H/V), gives new constraint on near-surface structure due to shallow crust sensitivity
- Shallow crust structures previously only seen in local studies are recovered regionally via joint inversion of phase velocity and H/V

Abstract

A self-consistent regional-scale seismic velocity model with resolution from seismogenic depth to the surface is crucial for seismic hazard assessment. Though Southern California is the most seismically imaged region in the world, techniques with high near-surface sensitivity have been applied only in disparate local areas and have not been incorporated into a unified model with deeper resolution. In the present work, we obtain isotropic values for Rayleigh wave phase velocity and ellipticity in Southern California by cross-correlating daily time-series from the year 2015 across 315 regional stations in period ranges 6 to 18 seconds. Leveraging the complementary sensitivity of the two Rayleigh wave datasets, we combine H/V and phase velocity measurements to determine a new 3D shear velocity model in a Bayesian joint inversion framework. The new model has greatly improved shallow resolution compared to the SCEC CVMS4.26 reference model. Well-known large-scale features common to previous studies are resolved, including velocity contrasts across the San Andreas, San Jacinto, Garlock, and Elsinore faults, mid-crustal high-velocity structure beneath the Mojave Desert, and shallow Moho beneath the Salton Trough. Other prominent features that have previously only been imaged in focused local studies include the correct sedimentary thickness of the southern Central Valley, fold structure of the Ventura and Oak Ridge Anticlines, and velocity contrast across the Newport-Inglewood fault. The new shallow structure will greatly impact simulation-based studies of seismic hazard, especially in the near-surface low-velocity zones beneath densely populated areas like the Los Angeles, San Bernardino, and Ventura Basins.

1 Introduction

Southern California is one of the most tomographically imaged regions in the world from a variety of methods including local body waves (e.g., Lin et al., 2010; Allam & Ben-Zion, 2012), teleseismic body waves (Schmandt & Humphreys, 2010), surface waves (Tanimoto & Prindle Sheldrake, 2002; Yang & Forsyth, 2006), ambient noise (e.g., Lin et al., 2008; Zigone et al., 2015; Barak et al., 2015), and full waveforms (e.g., Chen et al., 2007; Tape et al., 2009). The most recent models combining earthquake and ambient noise data (Lee et al., 2014; Fang et al., 2016) are extremely detailed and can successfully replicate observed earthquake waveforms at relatively high frequency (Taborda et al., 2016). However, one of the main limitations of these models is that they provide only weak constraint on the uppermost crustal structure (<3km) due to the relatively long periods employed (above a few seconds) and because amplitude information is not included. Shallow structure is well constrained by recent, focused active-source seismic or local earthquake double-difference tomography studies in a few sub-regions (e.g., Fuis et al., 2001; Süss & Shaw, 2003; Allam et al., 2014; Fuis et al., 2017), but is lacking regionally. Improved models of upper crustal structure are crucial because they allow vastly improved seismic ground motion predictions (Vidale and Helmberger, 1988; Graves et al., 2011), ameliorate misinterpretations of mantle structure (Waldhauser et al., 2002; Bozdağ and Trampert, 2008; Schulte-Pelkum & Ben-Zion, 2012), provide insight into lithospheric discontinuities (Langston, 2011), and validate geological interpretations based on surface observations (e.g., Graymer et al., 2005). Because Rayleigh wave horizontal-to-vertical (hereafter, denoted as H/V for conciseness) ratios have shallower sensitivity than phase velocity, they can provide much stronger constraints on shallow crustal structure at regional scales (Tanimoto & Rivera, 2008; Lin et al., 2012; Lin et al., 2014).

Surface wave tomography using phase or group velocities measured from ambient seismic noise cross-correlations is by now a standard technique (e.g., Bensen et al., 2007; Lin et al., 2009; Campillo et al., 2011). Traditional methods for measurement of noise spectral H/V ratio (e.g., Nakamura, 1989; Fäh et al., 2001) have been used to image structure in the upper few hundred meters, characterize site response, and predict ground motion. Interpretation of these measurements, however, depends on the assumed noise character, i.e. Rayleigh wave dominant, body wave dominant, or a mix (Bonnefoy-Claudet et al. 2006). Rayleigh waves isolated from the noise wavefield using noise cross-correlation, on the other hand, have been used to measure short period Rayleigh wave H/V ratios and recover shallow velocity structure across the U.S. (Lin et al., 2014). Recently, Rayleigh H/V ratios have been measured in Southern California and used to interpret shallow structure (Muir and Tsai, 2017). However, a joint 3D inversion for regional shear velocities incorporating both H/V data to constrain shallow structure and phase velocities to constrain the mid-crust has not been conducted.

In the present work, we leverage this complementary sensitivity of the Rayleigh wave amplitude and phase data to image the crustal shear wave velocity structure throughout Southern California. We perform detailed analysis of Rayleigh wave H/V ratio from noise cross-correlations on 315 stations and combine H/V and phase velocity measurements in a Markov Chain Monte Carlo joint inversion. This method benefits from the quantification of full model uncertainties and analysis of misfit while avoiding local minima by testing an ensemble of candidate models (Shen et al., 2012; Shen & Ritzwoller, 2016; Roy & Romanowicz, 2017). In Section 2, we describe the cross-correlation and measurement of H/V ratios, quality control criteria, and the Markov Chain Monte Carlo inversion methods. We present the results in Section 3 and discuss in detail the relevance of our final shear wave velocity model to the complicated geology of Southern California in Section 4.

2 Data & Methods

2.1 Data and Stations

From the Southern California Earthquake Data Center we obtain a year of continuous waveforms from 315 three-component stations available for 2015 in the Southern California plate boundary region (Figure 1). These stations are associated with multiple seismic networks including the Anza network, Southern California Seismic Network, and the San Jacinto Fault Zone network. From these networks, we incorporate multiple seismic instruments including broadband (BH, HH, BN, HN) and short period (EH). This data set allows us to analyze several geological regions of interest including the Coast Ranges, Central Valley, Mojave Desert, Sierra Nevada Range, Los Angeles Basin, San Jacinto Fault Zone, Peninsular Ranges, and the Salton Trough (Figure 1). Our study area also includes the Transverse Ranges, between the Coast Ranges, LA basin and the Mojave Desert, although this is not marked in Figure 1 in order to emphasize station coverage.

2.2 Ambient Noise Pre-Processing and Cross-Correlation

We closely follow the method described in Lin et al. (2014) to process the daily noise time series for each station prior to cross-correlation and stacking. For each station, data is cut into daily noise time series followed by decimation to a sampling rate of 4 Hz. We remove the mean, trend and instrument response for each east, north, and vertical component (E, N, Z) and apply a bandpass filter between 5 s and 150 s periods. Following Bensen et al. (2007), we next remove earthquake signals and instrumental irregularities via temporal normalization. To obtain the temporal normalization functions, we bandpass the seismic signal between 15 and 50 second period and calculate a 128-s time window running absolute mean for each component. For each point in time, we divide the three-component unfiltered time-series by the maximum of all temporal normalization functions for that corresponding time across all components (E, N, Z). Following temporal normalization, we perform spectral whitening to broaden the period band to increase potential recovery of surface-wave signals (Lin et al., 2008), dividing the spectrum of each component by the average amplitude of the three-component (E, N, Z) smoothed, 0.025 Hz (or 20 points halfwidth) running-mean, spectra. By applying the same temporal normalization and spectral whitening to each component (E, N, Z) we preserve the relative amplitude between components and allow rotation to be applied after cross-correlation and stacking. Due to the commutative nature of these normalization processes, we perform these steps pre-cross-correlation, which saves significant computational cost (Lin et al., 2008).

We next apply the methods of Lin et al. (2008) to calculate the nine-component cross-correlations among the north, east and vertical components, stack all daily cross-correlations from 2015, and rotate the horizontal motion into radial (R) and transverse (T) directions. After rotation, we analyze the positive time lag (causal) and negative time lag (acausal) parts independently to avoid potential mixing of good and bad signals. Figure 2a shows an example of the ZZ, ZR, RZ and RR cross-correlations bandpassed around 8 s period between a station in the LA Basin (FMP) and a station in the Sierra Nevada (WBS), highlighted in yellow and red, respectively, in Figure 1. Clear Rayleigh waves with similar arrival times are seen on all four components but the observed amplitudes are different, indicating contrasting horizontal-to-vertical ratios at each station site. The impact of asymmetric distribution of noise sources, normal to the coastline, due to oceanic waves dominating the noise field (Hillers et al., 2013) creates stronger signal on the positive time lag in Figure 2a due to the location of the virtual source (FMP) in relation to the receiver (WBS). We are still able to retrieve the empirical Green's function, detected through signal-to-noise ratio, with inhomogeneous noise distribution due to sufficiently strong ambient noise and its natural scattering properties (Yang & Ritzwoller, 2008; Lin et al., 2008).

The negative time derivative of the ZZ, ZR, RZ and RR cross-correlations, assuming a diffuse noise wavefield (Lobkis & Weaver, 2001), is related to the Rayleigh-wave Green's functions for a point force in the vertical (Z) or radial (R) direction at the source station and recorded in the vertical and radial directions at the receiver station. As shown in Figure 2b, by combining ZZ and ZR cross-correlations or RZ and RR cross-correlations, we can study the Rayleigh-wave particle motion at the second (acting as the receiver) station. Similarly, by combining ZZ and RZ cross-correlations or ZR and RR and considering the reciprocity of the Green's function (Aki & Richards 2002), we can analyze Rayleigh-wave particle motion at the first (acting as the source) station. As the wave is traveling from the source, FMP, to receiver, WBS, the receiver station shows retrograde particle motion. In contrast, the particle motion is prograde for the particle motion associated with the source station.

From Figure 2b it is apparent that the amplitude ratios differ strongly between the two stations; receiver station WBS is elongated vertically (low H/V), and receiver station FMP is elongated horizontally (high H/V). This is due to the highly localized sensitivity of Rayleigh wave horizontal to vertical (H/V) amplitude ratios to shallow structure. Station FMP is located in the LA Basin, where the contrast of soft sediment and bedrock elongates the radial component and creates a high horizontal to vertical (H/V) amplitude ratio. Receiver station WBS is located on crystalline rock, which without a pronounced shallow to deep velocity contrast creates a low H/V ratio. In order to image both shallow and mid-crustal structure throughout the area, we make measurements of both H/V and phase velocities from the cross-correlation functions over period ranges of 6-18 s and 6-16 s, respectively. The relative depth sensitivities for shear waves of phase velocities and H/V ratios are shown by their sensitivity kernels in Figure 3 for a location on the San Andreas fault (Fig. 1 green star). These sensitivity kernels demonstrate the complimentary sensitivity of the two Rayleigh wave measurements.

2.3 H/V

We use frequency-time analysis (FTAN; Bensen et al., 2007) to determine the maximum amplitude of the envelope for both causal and acausal sides of the ZZ, ZR, RZ and RR cross-correlations. Next, we measure H/V independently on both the causal and acausal portions of the correlograms. Specifically, for the first station (source station) we calculate H/V using RZ/ZZ and RR/ZR cross-correlation amplitude ratios for both the causal and acausal signals (i.e. four H/V measurements per station of each station pair). Similarly, for the second station (receiver station) H/V is determined using ZR/ZZ and RR/RZ cross-correlation amplitude ratios. We only retain good measurements by imposing several selection criteria, including signal-to-noise ratio greater than 5 and interstation distance larger than three wavelengths to satisfy the far-field condition (Bensen et al., 2007). For each period band, we define the signal-to-noise ratio as the average of the ratio of peak energy within the expected Rayleigh wave signal window, between 1.5km/s and 4.5km/s, to the root mean square of noise before and after the expected signal window (Lin et al., 2008). We apply this method to all cross-correlations to establish a large number of H/V measurements for each station.

We further stabilize each station's result in a quality control process designed to remove spurious measurements. We iteratively remove all measurements greater than three standard deviations, recomputing the mean and number of measurements within two standard deviations until no further measurements are discarded. The final range of measurements after stabilization is marked for stations FMP and WBS in Figure 4 via dashed lines. For each station, we then use H/V measurements retained after stabilization to calculate isotropic H/V and uncertainty as the mean and standard deviation of the mean for each station, respectively.

Because H/V is a measurement of the relative change of two quantities, we express both H/V and uncertainty as logarithms (Figure 5a,c); this has been shown to be the only symmetric, additive, and normed indicator of relative change (Törnqvist et al., 1985). Since H/V is a local measurement, we perform variable Gaussian smoothing to resolve log10(H/V) measurements throughout the entire region with 0.05º-by-0.05º spaced grid points (Fig. 5a,c) setting the maximum Gaussian half-width as distance to the three nearest stations. To prevent overly-smoothed results, we discard any points within the region that do not have three stations within 50km. To propagate uncertainty, we determine the gaussian-weighted uncertainty from the standard deviation of the mean H/V of stations within the defined Gaussian distance for each grid point (Fig. 5b,d).

2.4 Phase Velocities from Eikonal Tomography

We use the isotropic phase velocity (Vph) maps derived by Qiu et al. (2018) over the period range of 6 to 16 seconds. Rayleigh wave phase-velocity dispersion curves are first measured from vertical-vertical cross-correlations for all available station pairs in the same region as the present study (Figure 1). Eikonal tomography (Lin et al., 2009) is then performed to obtain apparent phase velocities using phase travel times over 0.05º-by-0.05º grid points for each virtual source and period. The quality of the derived phase velocity is improved by stacking phase velocities obtained from all available virtual sources. The resulting isotropic phase velocities increase with depth and are generally higher in mountainous regions, such as the Peninsular Ranges, and lower in basins, including the LA Basin, Salton Trough and Central Valley (Fig. 6a,c). The results are generally consistent with corresponding phase velocity measurements in the area based on beamforming analysis (Roux & Ben-Zion, 2017). Phase velocity uncertainty is determined based on the variation of measurements using different virtual sources (Fig. 6b,d).

2.5 Monte Carlo Joint Inversion

To jointly invert phase velocities and H/V ratios for shear wave velocity, we use a non-linear Bayesian Markov Chain Monte Carlo (MCMC) method. This method has several advantages: it fully explores the available parameter space, it is unlikely to be trapped in a local minimum, and can fully quantify model uncertainty (Shen et al., 2012; Roy and Romanowicz, 2017).

Following Shen et al. (2012), we assemble a starting model across Southern California with uniform horizontal 0.05º-by-0.05º spaced grid points based on the SCEC Community Velocity Model CVMS4.26 (Lee et al., 2014). At each grid point, we extract an independent 1D Vs model which we parameterize with three layers: a linear sedimentary layer near the surface, a crustal layer described by 10 cubic B-splines and the upper mantle defined by 5 cubic B-splines to a total depth of 50km. Our solution is inherently regularized due to the spatial discretization of the B-splines employed, which results in uncertainty of our final model to be underestimated (Dettmer et al., 2016). The thickness of the top linear layer is defined by the depth which the CVMS4.26 model reaches 2.3 km/s, roughly representing a sedimentary layer with linearly increasing Vs. The depth to the Moho is explicitly defined in the CVMS4.26. We choose to use 10 cubic B-splines in the crust to honor the often-presented complexity in the starting reference model. To decrease the number of parameters in our MCMC inversion, we only perturb the even number of the crustal spline value and using the mean of the neighboring spline perturbation to determine the odd number of the spline perturbation. This also allows our model to honor the basic structure resolved in the CVMS4.26 model (Lee et al., 2014). We hold the Moho depth and mantle splines completely fixed. Holding the mantle parameters fixed is a reasonable approach because the H/V and phase data at the periods we employ have very weak sensitivity below the crust (Fig. 3). In this study, we use the empirical relationships described by Brocher (2005) to determine Vp and density from the Vs models.

For each 1D model, we next create *a priori* distributions of the 8 free parameters: the Vs velocity values of the top and bottom of the sedimentary layer, sedimentary thickness, and 5 spline values in the crust. The prior distributions are centered around the starting model values and are obtained by the Gaussian probability distribution described in Table 1, where the Gaussian width of each parameter is empirically chosen to provide full sampling of the model space (Shen et al., 2012). These *a priori* distributions control the parameter space explored by the inversion.

We follow the Markov Chain Monte Carlo inversion described by Shen et al. (2012) to determine the posterior distribution from the prior distributions. Models are randomly selected from the prior distributions by simultaneously perturbing all eight parameters. The model misfit is then characterized as the χ^2 difference between the observed and the forward-calculated H/V and phase velocity of each model using the method of Herrmann et al. (2004). The χ^2 model misfit treats phase velocity and H/V measurements equally, where phase velocity and H/V uncertainty corresponds to 150% of the standard deviation of the mean for the associated measurement at each period. We use 150% of the standard deviation to account for potential systematic bias that is not encompassed by the measurement variation (Lin et al., 2012; Shen et al., 2013). Parameter space is then explored following the Metropolis algorithm (e.g., Mosegaard & Tarantola, 1995; Beichl et al., 2000). We obtain the likelihood functional of the model from forward computation using the Thomson-Haskell method, computed via Herrmann et al. (2004), with an earth-flattening transformation (Shen et al., 2012). If the probability of acceptance, related to the misfit of the model to the data through the likelihood function (Shen et al., 2012), is higher than the previous model we define a new perturbation from this model. If the model has poorer misfit we either instead define a new perturbation from the previous model or accept this realization. This decision is guided by a probability defined by the likelihood function and Metropolis law, as discussed in Shen et al. (2012), and prevents the inversion process from becoming trapped in a local minimum (Mosegaard & Tarantola, 1995). After 3000 iterations of random perturbations, we begin a new random set of model iterations from the original starting model. We perform 10 of these jumps with 3000 iterations per jump. To form the posterior distribution, we select all models with misfit less than or equal to 1.5 times the misfit of the absolute lowest misfit model. This estimation of the posterior distribution is computationally efficient and effectively removes models that may have been accepted during the inversion prior to the equilibrium state, which describes the posterior model distribution. However, by doing so we also effectively trim our posterior distribution and underestimate true posterior distribution width. The model created by the mean of each parameter of models within the posterior distribution is our final model. To obtain a full 3D model across Southern California, we perform this inversion independently for each 0.05ºx0.05º grid point.

To increase inversion stability, we add a few reasonable constraints: the maximum Vs in the crust is 4.9 km/s, the sedimentary layer must have increasing Vs with depth, the first two splines in the crust must be increasing, and a positive change in velocity must exist across the (top sedimentary) linear layer to the (middle) crustal layer. The mean number of accepted posterior models for each 1-dimensional inversion is 136 models. Example MCMC inversions for two grid points are shown in Figures 7 and 8 (locations are shown with a green and blue star each in Figure 1). This includes the starting model formed from the CVMS, the entire model space searched, posterior models, the final mean result and associated standard deviation (Figures 7a & 8a). Additionally, the forward model results of H/V and phase velocity are shown for the data, the starting model, all posterior models and the final mean model (Figures 7b,c & 8b,c). Finally, the distributions of posterior compared to prior parameters are shown for several different parameters (Figures 7d,e,f & 8d,e,f). From these distributions it is evident that our final results show a narrow Gaussian distribution and are sensitive to the shallow and mid-crust shear wave velocity.

3 Results

3.1 H/V and Phase Velocity Results

The map-view images of H/V and phase velocity (Figures 5a,c and 6a,c) show consistent patterns related to geologic structure. Regions of high H/V and low phase velocity correspond to sedimentary basins including the LA Basin, Central Valley and Salton Trough, and the size of these features decreases with increasing period (corresponding to depth). Regions with low H/V and high phase velocity correspond to mountainous regions, including the Sierra Nevada and

Peninsular Ranges. Major faults including the San Andreas, San Jacinto, and Garlock faults, appear as sharp boundaries separating regions of different velocity and H/V.

The corresponding uncertainty maps (Figures. 5b,d and 6b,d) provide confidence in the derived phase velocity and H/V data. We see a decrease of uncertainty with increase in period for H/V and phase velocity, with uncertainties less than 5% at all periods. Specifically, we observe variations in uncertainty up to 5% with most uncertainties less than 2% for phase velocity, but slightly higher variations in H/V uncertainties, up to 7% at shorter periods, with most uncertainties less than 5%. Higher uncertainties over lower periods is likely due to stronger heterogeneity and wavefield complexity, such as multipathing and off-great-circle propagation, in the shallow structure. Both datasets have relatively higher uncertainty near the edges of the region, which may be attributed to poorer station distribution and azimuthal coverage. Observations of high uncertainties at low periods for both datasets in basin areas (e.g., Salton Trough, LA Basin, Central Valley) may be due to strong 3D heterogeneity effects in the shallow structure. In order to account for underestimation of uncertainty in our measurements, we use 150% of the measured uncertainty for both phase velocity and H/V in the joint inversion.

3.2 Monte Carlo Inversion 1-D Results

Figures 7 and 8 summarize the 1D inversion results for two different locations: the San Gorgonio Pass and the Central Valley respectively. By using a starting model that predicts the phase velocity dispersion fairly accurately, we are able to search the full model space and find a suite of best-fitting models to form the posterior. In both example cases, the starting model performs poorly at predicting H/V ratio. This is because the CVMS4.26 model (Lee et al., 2014) was developed using data with limited sensitivity to the shallow structure (e.g. the top 3 km). The inclusion of H/V data in the present work leads to strong changes in the shallow structure (<10km depth), which dramatically improves H/V fit in addition to slightly improving phase velocity fit. In nearly all cases, changes related to higher H/V in the data than the starting model correspond to low velocity zones in the upper few km that are completely absent in the starting model, especially near the Salton Trough, Coast Ranges and Indian Wells Valley, as discussed in Section 4. Because of the shallow sensitivity of the datasets, we do not constrain structure below ~25km depth; the posterior distributions are quite broad and simply average back to the starting model below this depth. Comparing prior and posterior model distributions (Figures 7d,e,f and 8d,e,f) indicates that the posterior models lie completely within the examined parameter space, are much more tightly constrained by the data than the prior distributions, and generally follow Gaussian distributions. In addition, the posterior distributions become wider with depth, indicating a relative decrease in model certainty as expected.

3.3 Shear Velocity in 3D

The joint inversion results in terms of both absolute velocity and relative change to the starting model CVMS4.26 are presented in Figures 9 and 11, and the distribution of misfit values is displayed in Figure 10. We also include corresponding plots in the Supporting Information Section (Figures S1-S3) that compare our joint inversion results to the SCEC Community Velocity Model – Harvard. Specifically, map-view slices at several depths are shown in Figure 9, and seven cross-sections are shown in Figure 11. The map-view images have no smoothing applied after the individual 1D inversions, while the cross-sections were created using narrow-width cubic interpolation to sample along the arbitrarily-oriented profiles (Figure 9e). The final model shows the strongest changes from the starting model at shallow depths due to the addition of H/V ratios in the inversion. These H/V data in general require lower velocities near the surface (<2km depth) and higher velocities in the upper crust compared to the starting model. The correspondence of the absolute velocity structure to various geological provinces is discussed in detail in Section 4.

The total χ^2 misfit at each grid point for both the starting and final models is shown in map view for each dataset (Figure 10). The final model improves fit of both phase velocity and H/V compared to the starting model. In general, misfit of the final model is low (< 1.5), except for the Los Angeles basin and in a few localized areas at the edges of the imaged region. This relatively high misfit in the LA basin is potentially due to the Moho being fixed at an incorrect depth in the present work; results from a recent dense seismic array indicate that the Moho beneath the LA basin is much shallower than previously thought (Ma & Clayton, 2016). Nevertheless, the new joint inversion model features significantly better fits to the data than the CVM-S starting model, including in the LA basin.

4 Discussion

We provide interpretations of the 3D joint inversion model in the context of the various geological provinces of Southern California. Though a comprehensive interpretation of a seismic velocity model in terms of geology requires consideration of a variety of additional parameters such as temperature, fluid content, fracture density, and Poisson's ratio (e.g., Christensen, 1996; Karato & Jung, 1998), we note the strong correspondence of the present model to previous results and to expectations based on geological inferences.

4.1 Southern Central Valley and Sierra Nevada

At 0.5 and 2 km depth (Figure 9a,b), a prominent feature in our result is the transition from the slower sediments in the Central Valley to the faster Sierra Nevada foothills. This transition is consistent with previous tomographic imaging results (Tape et al., 2010; Lee et al., 2014). However, the improved shallow sensitivity provided by the H/V data leads to a reduced sediment thickness (3-4km deep) in the southern tip of the Central Valley (F-F') which more closely matches the active-source studies (Fliedner et al., 2000) and focused ambient noise imaging studies (Fletcher & Erdem, 2017). As evident in Figure 9(a), to the east of the Sierra Nevada range and north of the Garlock fault is a low-velocity zone in the Indian Wells Valley, which has previously been imaged as a shallow (<3km) feature (Tape et al., 2010) that may host enhanced hydrothermal activity (Ho-Liu et al., 1988).

4.2 Coast Ranges and Transverse Ranges

The Coast Ranges, west of the Central Valley, are very slow with similar velocities to the Central Valley (Figure 9). This has been observed in previous studies (Tape et al., 2010) and attributed to stacking of Miocene and younger sediments caused by East-West shortening along various active structures (Namson & Davis, 1988). At 0.5 km depth, the Transverse Ranges and surrounding areas have blocks of varying slow velocities corresponding to major faults including the San Gabriel fault, San Cayetano fault and San Andreas fault (A-A'). The southern San Andreas fault has clear velocity contrasts with opposite polarities to the NW and SE of San Gorgonio. These features were observed with fault zone head waves and previous tomographic results and can have important implications for the size and directivity of large earthquakes on the southern San Andreas fault (Share & Ben-Zion, 2016). Evidence of fold and thrust belts corresponding to the Ventura anticline and San Cayetano fault can be seen to the southwest of the San Cayetano fault surface trace, and supports the model proposed by Hubbard et al. (2014). The San Cayetano fault also bounds a fast 5km feature (F-F') and marks the eastern edge of slow, shallow sediments which transition to much faster crystalline rocks (Powell, 1981) bounded to the east by the San Andreas fault.

4.3 Mojave Desert

The Mojave Desert is bounded by the Garlock fault to the north and the San Andreas fault to the southwest (Fig. 1). South of the Sierra Nevada range, the Garlock fault separates the faster mountains from slower material in Antelope Valley in the westernmost edge of the Mojave, as seen at very shallow depths (Figure 9a). Contrastingly, at 2km depth, Antelope Valley is faster than the Sierra Nevada range, north of the Garlock fault, or the region south of the San Andreas fault. Previous active-source studies (Lutter et al., 2004) have also shown that this shallow valley (G-G') contains slow material overlying fast material.

This trend is also seen in the CVMS, but is deeper than the new model (Figure 9 d,e). Mid-crustal structure beneath the Mojave Desert is known to be strongly anisotropic (e.g., Louie & Clayton, 1987) due to complicated Miocene metamorphic processes (Fletcher et al., 1995). Additionally, velocity contrasts are seen across the Eastern California Shear Zone similar to previous results (Tape et al., 2010; Lee et al., 2014). The northeastern part of the Mojave (A-A') has slower material near the surface overlying the shallow fast material beginning at the Lockhart fault. At 9km depth, the region south of the Garlock fault appears slower than the material in the Sierra Nevada mountains north of the Garlock fault, similar to previous results (e.g.,Tape et al., 2010).

4.4 Los Angeles Basin

Los Angeles is underlain by a well-studied basin with a mean depth of ~5km and maximum depth of 10km (Magistrale et al., 1996) that has been developing since at least the Middle Miocene (Ingersoll & Rumelhart, 1999). The internal structure of the basin is complicated by multiple east-west trending active blind thrust faults (Shaw et al., 2015) with complex patterns of interaction (Rollins, 2018). The LA Basin in the new model has the lowest velocities in the entire region, though it is also the region with the highest residual misfit (Fig. 10) likely due to the incorrectly constrained Moho (Ma & Clayton, 2016) as described in Section 3.3. The overall basin structure (B-B' and G-G') is generally consistent with CVMS-4.26, though with much lower velocities at depths less than 2km as required by the H/V data. These lower velocities are crucial to correctly quantify seismic hazard (e.g., Olsen, 2000) in the LA Basin, the most populous region in Southern California with some of the highest seismic risk in the United States (e.g., Petersen et al., 2015).

There are clear velocity changes across the Newport-Inglewood fault (B-B', 1-3km depth), which have previously been observed in more detailed studies (Lin et al., 2013). The basin deepens between the Newport-Inglewood and Whitter faults, in line with previous geological (Shaw & Suppe, 1996) and geochemical (Boles et al., 2015) studies. Additionally, there is a strong contrast across the Whitter fault leading to a shallower basin NE of the fault as expected from the fault throw (Davis et al., 1989; Shaw et al., 2015). The basin is bounded sharply to the North by the Sierra Madre fault (B-B', G-G'), an active reverse fault largely responsible for the uplift of the San Gabriel Mountains (Shen et al., 2011).

4.5 San Bernardino Basin and Major Faults

The San Bernardino basin is a shallow (<2km; Anderson et al., 2004) feature bounded to the east by the San Andreas Fault and to the west by the San Jacinto Fault zone (Fig 9a). To the southeast of the basin is a region of small-scale faults likely responsible for transfer of stress from the southern San Andreas fault to the more favorably oriented San Jacinto fault (Langenheim et al., 2004; Fialko, 2006). The San Jacinto bounds some of the strongest across-fault contrasts in the entire model, as seen in previous tomographic studies (Tape et al., 2010; Allam & Ben-Zion, 2012; Allam et al., 2014). This relatively fast region is composed of Cretaceous plutons (Morton & Kennedy, 2005) and is also sharply bounded to the SW by the Elsinore fault (C-C', D-D'). The sense of the velocity contrast changes from SW-fast to NE-fast southward along the fault due to the presence of the large San Jacinto plutons (Hill, 1988). The sharp across-fault velocity contrasts can lead to a preference for NW-propagating earthquake ruptures (Shi & Ben-Zion, 2006; Allam et al., 2014), which can be up to M7.5 based on paleoseismic data (Rockwell et al., 2015).

4.6 Salton Trough and Peninsular Ranges

The Peninsular Ranges in far southwestern California are composed of a series of large-scale Mesozoic plutonic rocks (Gastil, 1975; DePaolo, 1981) that are almost completely unfaulted (Plesch et al., 2007). Bounded to the east by the Elsinore fault, the Peninsular Ranges have the fastest shallow velocities in the present model (Figure 9a), in agreement with previous regional tomographic studies (Tape et al., 2010; Lee et al., 2014). To the east is the Salton Trough, a region of crustal extension (Sylvester & Smith, 1976) with an extremely shallow Moho (Ozakin & Ben-Zion, 2015) possibly indicating incipient mid-ocean spreading centers (Robinson et al., 1972; Han et al., 2016). The Salton Trough in the present model is much wider and slower in the upper few km (Figure 9a; Figure 11 E-E') than the CVMS4.26, in agreement with previous active-source studies (Livers et al., 2012; Fuis et al., 2017; Han et al., 2016). The Superstition Hills fault and Brawley Seismic zone have no obvious signal in the seismic velocity model, supporting the idea that these are regions of distributed deformation due to multiple fault strands (Hudnut et al., 1989) and diffuse seismicity (Geng et al., 2013).

5 Conclusions

We combine Rayleigh-wave H/V ratios and phase velocity measurements in a joint Bayesian inversion to determine a regional shear velocity model for Southern California with improved resolution in the surface, shallow and upper crustal structure. Previous models such as the CVMS4.26 (Lee et al., 2014) have incorporated information from ambient noise and full waveforms but did not incorporate amplitude information and therefore have a relatively weak constraint on structure above 3km depth. By combining H/V ratios and phase velocity measurements, we gain sensitivity to shallow and mid-crustal shear velocity structure. The obtained large-scale mid-crustal features are similar to previous high-resolution models (e.g., Tape et al., 2010; Lee et al., 2014; Barak et al., 2015; Fang et al., 2016), lending confidence in the new model overall. The main improvement is the addition of new shallow features in the updated model, including more accurate basin depths and other near-surface low-velocity zones that have strong implications for studies of seismic hazard. The final model is a self-consistent regional-scale seismic velocity model with resolution from seismogenic depth to the surface.

In addition to resolving large-scale features of the crust, our shear velocity model includes small-scale shallow structure previously only seen by local imaging studies (Allam et al., 2014; Fliedner et al., 2000; Lin et al., 2013; Fuis et al., 2017). In the north this includes the shallower-sediments in the southern tip of the Central Valley (Fliedner et al., 2000; Fletcher & Erdem, 2017), high velocity of the Sierra Nevada Range (Tape et al., 2010), shallow slow velocities in the Coast and Transverse Ranges (Tape et al., 2010) and evidence of fold and thrust faults (Hubbard et al., 2014). We resolve similar shallow structure in the LA basin to the CVMS4.26 (Lee et al., 2014) while also imaging the Newport-Inglewood fault (Lin et al., 2013) and Whittier faults (Shaw and Suppe, 1996). We also are able to see the San Bernardino basin and differing velocity structure across the Elsinore, San Jacinto and San Andreas faults (Allam et al., 2014; Allam and Ben-Zion, 2012; Zigone et al., 2015). In the southern end of the region, we recover the Salton Trough and Peninsular Range with similar structure to active source studies (Livers et al., 2012; Fuis et al., 2017; Han et al., 2016). Our results demonstrate the considerable improvement to ambient noise imaging that can be gained from the incorporation of spatially dense Rayleigh wave H/V measurements to constrain shallow structure.

Acknowledgments

The data used in this work are archived and distributed by the Southern California Earthquake Data Center (SCEDC; http://scedc.caltech.edu/research-tools/waveform.html) and the IRIS Earthquake Data Center (https://ds.iris.edu/ds/nodes/dmc/). Both the SCEC Community Velocity Models used in this work, CVMS-4.26 and CVMH-15.1.0, are available from the Southern California Earthquake Center (https://github.com/SCECcode/UCVMC). This study was supported by the Southern California Earthquake Center (award #17195), National Science Foundation (grants CyberSEES-1442665, EAR-162061) and the King Abdullah University of Science and Technology (award OCRF-2014-CRG3-2300).

We also thank the reviewers of this paper, an anonymous individual and Dr. Jan Dettmer, for their valuable insight and constructive reviews of the manuscript.

The 3-D shear wave velocity model will be available from IRIS Data Services Products: Earth Model Collaboration (https://ds.iris.edu/ds/products/emc/).

References

Aki, K., & Richards, P. G. (2002). *Quantitative Seismology.* (2nd Ed.) Mill Valley, CA: University Science Books.

Allam, A.A., & Ben-Zion, Y. (2012). Seismic velocity structures in the southern California plateboundary environment from double-difference tomography. *Geophysical Journal International*, *190*, 1181-1196. https://doi.org/10.1111/j.1365-246X.2012.05544.x

Allam, A. A., Ben-Zion, Y., Kurzon, I., & Vernon, F. (2014). Seismic velocity structure in the Hot Springs and Trifurcation areas of the San Jacinto fault zone, California, from double-difference tomography. *Geophysical Journal International*, *198(2)*, 978–999. https://doi.org/10.1093/gji/ggu176

Anderson, M., J. Matti, & Jachens, R. (2004). Structural model of the San Bernardino basin, California, from analysis of gravity, aeromagnetic, and seismicity data. *Journal of Geophysical Research: Solid Earth*, *109*, B04404, 1-20. https://doi.org/10.1029/2003JB002544

Barak, S., Klemperer, S. L., & Lawrence, J. F. (2015). San Andreas Fault dip, Peninsular Ranges mafic lower crust and partial melt in the Salton Trough, Southern California, from ambient-noise tomography. *Geochemistry Geophysics Geosystems*, *16*, 3946-3972.

Bensen, G.D., Ritzwoller, M. H., Barmin, M. P., Levshin, A. L. , Lin, F., Moschetti, M. P., Shapiro, N. M. , & Yang, Y. (2007). Processing seismic ambient noise data to obtain reliable broad-band surface wave dispersion measurements. *Geophysical Journal International*, *169*(3), 1239–1260. https://doi.org/10.1111/j.1365-246X.2007.03374.x

Boles, J. R., Garven, G., Camacho, H., & Lupton, J. E. (2015). Mantle helium along the Newport-Inglewood fault zone, Los Angeles basin, California: A leaking paleo-subduction zone. *Geochemistry, Geophysics, Geosystems*, *16*, 2364–2381. https://doi.org/10.1002/2015GC005951.

Bonnefoy-Claudet, S., Cotton, F., & Bard, P. (2006). The nature of noise wavefield and its applications for site effects studies: A literature review. *Earth-Science Reviews*, *79*(3-4), 205-227. https://doi.org/10.1016/j.earscirev.2006.07.004.

Bozdağ, E., & Trampert, J. (2008). On crustal corrections in surface wave tomography. *Geophysical Journal International*, *172*. 1066–1082. https://doi.org/10.1111/j.1365-246X.2007.03690.x

Brocher, T. (2005). Empirical relations between elastic wavespeeds and density in the Earth's crust. *Bulletin of the Seismological Society of America*, *95*(6), 2081–2092. https://doi.org/10.1785/0120050077

Campillo, M., Roux, P., & Shapiro, N. M. (2011). Seismic, Ambient Noise Correlation. In H. K. Gupta (Ed.), *Encyclopedia of Solid Earth Geophysics* (pp. 1230–1236). Dordrecht, Netherlands: Springer. https://doi.org/10.1007/978-90-481-8702-7_218

Chen, P., Zhao, L., & Jordan, T.H. (2007). Full 3D tomography for the crustal structure of the Los Angeles region. *Bulletin of the Seismological Society of America* , *97*(4), 1094-1120. https://doi.org/10.1785/0120060222

Christensen, N. I. (1996). Poisson's ratio and crustal seismology. *Journal of Geophysical Research: Solid Earth*, *101*(B2), 3139-3156. https://doi.org/10.1029/95JB03446

Davis, T. L., Namson, J., & Yerkes, R.F. (1989). A cross section of the Los Angeles Area: Seismically active fold and thrust belt, The 1987 Whittier Narrows earthquake, and earthquake hazard. *Journal of Geophysical Research: Solid Earth*, *94*(B7), 9644–9664. https://doi.org/10.1029/JB094iB07p09644

Dettmer, J., Hawkins, R., Cummins, P. R., Hossen, J., Sambridge, M., Hino, R., & Inazu, D. (2016). Tsunami source uncertainty estimation: The 2011 Japan tsunami. *Journal of Geophysical Research: Solid Earth*, *121*(6), 4483-4505. https://doi.org/10.1002/2015JB012764

DePaolo, D. J. (1981). A neodymium and strontium isotopic study of the Mesozoic calc‐alkaline granitic batholiths of the Sierra Nevada and Peninsular Ranges, California. *Journal of Geophysical Research: Solid Earth*, *86*(B11), 10470–10488, https://doi.org/10.1029/JB086iB11p10470

Fäh, D., Kind, F., & Giardini, D. (2001). A theoretical investigation of average H/V ratios. *Geophysical Journal International*, *145*, 535-549. https://doi.org/10.1046/j.0956-540x.2001.01406.x.

Fang, H., Zhang, H., Yao, H., Allam, A., Zigone, D., Ben-Zion, Y., et al. (2016). A new algorithm for three-dimensional joint inversion of body wave and surface wave data and its application to the Southern California plate boundary region. *Journal of Geophysical Research: Solid Earth*, *121*(5), 3557-3569. https://doi.org/10.1002/2015JB012702

Fialko, Y. (2006). Interseismic strain accumulation and the earthquake potential on the southern San Andreas fault system. *Nature*, *441*, 968-971. https://doi.org/10.1038/nature04797

Fletcher, J. M., Bartley, J. M., Martin, M. W., Glazner, A. F., & Walker, J. D. (1995). Large-magnitude continental extension: An example from the central Mojave metamorphic core complex. *Geological Society of America Bulletin*, *107*(12), 1468-1483. https://doi.org/10.1130/0016-7606(1995)107<1468:LMCEAE>2.3.CO;2

Fletcher, J. B., & Erdem, J. (2017). Shear-wave Velocity Model from Rayleigh Wave Group Velocities Centered on the Sacramento/San Joaquin Delta. *Pure and Applied Geophysics*, *174*(10), 3825–3839. http://doi.org/10.1007/s00024-017-1587-x

Fliedner, M. M., Klemperer, S. L., & Christensen, N. I. (2000). Three-dimensional seismic model of the Sierra Nevada arc, California, and its implications for crustal and upper mantle composition. *Journal of Geophysical Research*, *105*(B5), 10899-10921. https://doi.org/10.1029/2000JB900029

Fuis, G. S., Bauer, K., Goldman, M. R., Ryberg, T., Langenheim, V. E., Scheirer, D. S., et al. (2017). Subsurface Geometry of the San Andreas Fault in Southern California: Results from the Salton Seismic Imaging Project (SSIP) and Strong Ground Motion Expectations. *Bulletin of the Seismological Society of America*, *107*(4), 1642–1662. https://doi.org/10.1785/0120160309

Fuis, G. S., Ryberg, T., Godfrey, N. J., Okaya, D. A., & Murphy, J. M. (2001). Crustal structure and tectonics from the Los Angeles basin to the Mojave Desert, southern California. *Geology*, *29*(1), 15–18. https://doi.org/10.1130/0091-7613(2001)029<0015:CSATFT>2.0.CO;2

Gastil, R. G. (1975). Plutonic zones in the Peninsular Ranges of southern California and northern Baja California. *Geology*, *3*(7), 361–363. https://doi.org/10.1130/0091-7613(1975)3<361:PZITPR>2.0.CO;2

Geng, J., Bock, Y., Melgar, D., Crowell, B.W., & Haase, J.S. (2013). A new seismogeodetic approach applied to GPS and accelerometer observations of the 2012 Brawley seismic swarm: Implications for earthquake early warning. *Geochemistry*, *Geophysics*, *Geosystems*, *14*(7), 2124–2142. http://doi.org/10.1002/ggge.20144

Graves, R., Jordan, T. H., Callaghan, S., Deelman, E., Field, E., Juve, G., et al. (2011). CyberShake: A Physics-Based Seismic Hazard Model for Southern California. *Pure and Applied Geophysics*, *168*(3), 367–381. http://doi.org/10.1007/s00024-010-0161-6

Graymer, R. W., Ponce, D. A., Jachens, R. C., Simpson, R. W., Phelps, G. A., & Wentworth, C. M. (2005). Three-dimensional geologic map of the Hayward fault, northern California: Correlation of rock units with variations in seismicity, creep rate, and fault dip. *Geology*, *33*(6), 521–524. https://doi.org/10.1130/G21435.1

Han, L., Hole, J. A., Stock, J. M., Fuis, G. S., Kell, A., Driscoll, N.W, et al. (2016). Continental rupture and the creation of new crust in the Salton Trough rift, Southern California and northern Mexico: Results from the Salton Seismic Imaging Project. *Journal of Geophysical Research: Solid Earth*, *121*(10), 7469–7489. https://doi.org/10.1002/2016JB013139

Herrmann, R.B. & Ammon, C.J. (2004). Surface waves, receiver functions and crustal structure, in Computer Programs in Seismology, Version 3.30, Saint Louis University, http://www.eas.slu.edu/People/RBHerrmann/CPS330.html.

Hill, R. I. (1988). San Jacinto intrusive complex: 1. Geology and mineral chemistry, and a model for intermittent recharge of tonalitic magma chambers. *Journal of Geophysical Research: Solid Earth*, *93*(B9), 10325-10348. https://doi.org/10.1029/JB093iB09p10325

Hillers, G., Ben‐Zion, Y., Landes, M., & Campillo, M. (2013). Interaction of microseisms with crustal heterogeneity: A case study from the San Jacinto fault zone area. *Geochemistry, Geophysics, Geosystems*, *14*(7), 2182-2197. https://doi.org/10.1002/ggge.20140

Ho‐Liu, P., Kanamori, H., & Clayton, R. W. (1988). Applications of attenuation tomography to Imperial Valley and Coso-Indian Wells Region, southern California. *Journal of Geophysical Research: Solid Earth*, *93*(B9), 10501-10520. https://doi.org/10.1029/JB093iB09p10501

Hubbard, J., Shaw, J. H., Dolan, J. F., Pratt, T. L., McAuliffe, L. J., & Rockwell, T. K. (2014). Structure and seismic hazard of the Ventura Avenue anticline and Ventura fault, California: Prospect for large, multisegment ruptures in the Western Transverse Ranges. *Bulletin of the Seismological Society of America*, *104*(3), 1070–1087. http://doi.org/10.1785/0120130125

Hudnut, K., Seeber, L., Rockwell, T., Goodmacher, J., Klinger, R., Lindvall, S., & McElwain, R. (1989). Surface ruptures on cross-faults in the 24 November 1987 Superstition Hills, California, earthquake sequence. *Bulletin of the Seismological Society of America*, *79*(2), 282–296.

Ingersoll, R. V, & Rumelhart, P. E. (1999). Three-stage evolution of the Los Angeles basin, southern California. *Geology*, *27*(7), 593–596. https://doi.org/10.1130/0091-7613(1999)027<0593:TSEOTL>2.3.CO;2

Karato, S., & Jung, H. (1998). Water, partial melting and the origin of the seismic low velocity and high attenuation zone in the upper mantle. *Earth and Planetary Science Letters*, *157*(3-4), 193-207. https://doi.org/10.1016/S0012-821X(98)00034-X

Langston, C. A. (2011). Wave-Field Continuation and Decomposition for Passive Seismic Imaging Under Deep Unconsolidated Sediments. *Bulletin of the Seismological Society of America*, *101*(5), 2176–2190. https://doi.org/10.1785/0120100299

Langenheim, V. E., Jachens, R. C., Morton, D. M., Kistler, R. W., & Matti, J. C. (2004). Geophysical and isotopic mapping of preexisting crustal structures that influenced the location and development of the San Jacinto fault zone, southern California. *Bulletin of the Geological Society of America*, *116*(9–10), 1143–1157. https://doi.org/10.1130/B25277.1

Lee, E. J., Chen, P., Jordan, T. H., Maechling, P. B., Denolle, M. A., & Beroza, G. C. (2014). Full-3-D tomography for crustal structure in southern California based on the scattering-integral and the adjoint-waveform methods. *Journal of Geophysical Research: Solid Earth*, *119*(8), 6421-6451. https://doi.org/10.1002/2014JB011346

Lin, F. C., Li, D., Clayton, R. W., & Hollis, D. (2013). High-resolution 3D shallow crustal structure in Long Beach, California: Application of ambient noise tomography on a dense seismic arrayNoise tomography with a dense array. *Geophysics*, *78*(4), Q45-Q56. https://doi.org/10.1190/geo2012-0453.1

Lin, F.-C., Moschetti, M. P., & Ritzwoller, M. H. (2008). Surface wave tomography of the western United States from ambient seismic noise: Rayleigh and Love wave phase velocity maps. *Geophysical Journal International*, *173*, 281-298. https://doi.org/10.1111/j.1365-246X.2008.03720.x

Lin, F.-C., Ritzwoller, M.H, & Snieder, R. (2009). Eikonal tomography: surface wave tomography by phase front tracking across a regional broad-band seismic array. *Geophysical Journal International*, *177*(3), 1091-1110, https://doi.org/10.1111/j.1365-246X.2009.04105.x

Lin, F.-C., Schmandt, B., & Tsai, V. C. (2012). Joint inversion of Rayleigh wave phase velocity and ellipticity using USArray: Constraining velocity and density structure in the upper crust. *Geophysical Research Letters*, *39*(L12303), 1-7. https://doi.org/10.1029/2012GL052196.

Lin, F.-C., Tsai, V. C., Schmandt. B. (2014). 3-D crustal structure of the western United States: application of Rayleigh-wave ellipticity extracted from noise cross-correlations. *Geophysical Journal International*, *198*(2), 656-670. https://doi.org/10.1093/gji/ggu160

Lin, G., Thurber, C.H., Zhang, H., Hauksson, E., Shearer, P. M., Waldhauser, et al. (2010). A California statewide three-dimensional seismic velocity model from both absolute and differential times. *Bulletin of the Seismological Society of America*, *100*(1), 225-240. https://doi.org/10.1785/0120090028

Livers, A. J., Han, L., Delph, J., White-Gaynor, A., Petit, R., Hole, J. A., et al. (2012). Tomographic characteristics of the northern geothermally active rift zone of the Imperial Valley and its rift margins: Salton Seismic Imaging Project (SSIP). *AGU Fall Meet. Abstr.*

Lobkis, O. I., & Weaver, R. L. (2001). On the emergence of the Green's function in the correlations of a diffuse field. *The Journal of the Acoustical Society of America*, *110*(6), 3011–3017. http://doi.org/10.1121/1.1417528

Louie, J. N. & Clayton, R. W. (1987). The nature of deep crustal structures in the Mojave Desert, California. *Geophysical Journal of the Royal Astronomical Society*, *89*. 125-132. https://doi.org/10.1111/j.1365-246X.1987.tb04398.x

Lutter, W. J., Fuis, G. S., Ryberg, T., Okaya, D. A., Clayton, R. W., Davis, P. M., et al. (2004). Upper crustal structure from the Santa Monica Mountains to the Sierra Nevada, Southern California: Tomographic results from the Los Angeles Regional Seismic Experiment, Phase II (LARSE II). *Bulletin of the Seismological Society of America*, *94*(2), 619–632. http://doi.org/10.1785/0120030058

Ma, Y. & Clayton, R.W (2016). Structure of the Los Angeles Basin from ambient noise and receiver functions. *Geophysical Journal International*, *206*(3), 1645–1651. https://doi.org/10.1093/gji/ggw236

Magistrale, H., McLaughlin, K., & Day, S. (1996). A geology-based 3D velocity model of the Los Angeles basin sediments. *Bulletin of the Seismological Society of America*, *86*(4), 1161–1166.

Mosegaard, K. and Tarantola, A., 1995. Monte Carlo sampling of solutions to inverse problems. *Journal of Geophysical Research: Solid Earth*, *100*(B7), pp.12431-12447.

Morton, D. M. & Kennedy, M. P. (2005). *Preliminary Geologic Map of the Sage 7.5' Quadrangle, Riverside County, California* (Map No. 2005-1285). United States Geological Survey. http://pubs.usgs.gov/of/2005/1285/

Muir, J. B., & Tsai, V. C. (2017). Rayleigh wave H/V via noise cross-correlation in southern California. *Bulletin of the Seismological Society of America, 107,* 2021-2027. https://doi.org/10.1795/0120170051.

Nakamura, Y. (1989). A method for dynamic characteristics estimation of subsurface using microtremor on the ground surface. *Quarterly Report of RTRI (Railway Technical Research Institute) (Japan), Vol 30*.

Olsen, K. B. (2000). Site amplification in the Los Angeles basin from three-dimensional modeling of ground motion. *Bulletin of the Seismological Society of America*, *90*(6B), S77-S94. https://doi.org/10.1785/0120000506

Ozakin, Y., & Y. Ben-Zion, 2015, Systematic receiver function analysis of the Moho geometry in the Southern California plate-boundary region, *Pure Appl. Geophys.*, 172, 1167-1184, doi:10.1007/s00024-014-0924-6.

Petersen, M. D., Moschetti, M. P., Powers, P. M., Mueller, C. S., Haller, K. M., Frankel, A. D., et al. (2015). The 2014 United States national seismic hazard model. *Earthquake Spectra*, *31*(S1), S1-S30. https://doi.org/10.1193/120814EQS210M

Plesch, A., Shaw, J. H., Benson, C., Bryant, W. A., Carena, S., Cooke, M., et al. (2007). Community fault model (CFM) for southern California. *Bulletin of the Seismological Society of America*, *97*(6), 1793-1802. https://doi.org/10.1785/0120050211

Powell, R. E. (1981). *Geology of the crystalline basement complex, eastern Transverse Ranges, southern California: Constraints on regional tectonic interpretation* (Doctoral dissertation, California Institute of Technology). Retrieved from CaltechTHESIS (http://resolver.caltech.edu/CaltechETD:etd-07252007-135803). Pasadena, CA: California Institute of Technology

Qiu, H., Ben-Zion, Y., & Lin, F.-C. (2018). Eikonal Tomography of the Southern California Plate Boundary Region. Abstract of the Annual Meeting of the American Geophysical Union.

Rockwell, T. K., Dawson, T. E., Ben-Horin, J. Y., & Seitz, G. (2015). A 21-event, 4,000-year history of surface ruptures in the Anza seismic gap, San Jacinto Fault, and implications for long-term earthquake production on a major plate boundary fault. *Pure and Applied Geophysics*, *172*(5), 1143-1165. https://doi.org/10.1007/s00024-014-0955-z

Rollins, J. C. (2018). *Using Heterogeneous 3D Earth Models to Constrain Interseismic and Postseismic Deformation in Southern California and Nepal* (Doctoral dissertation, California Institute of Technology). Retrieved from CaltechTHESIS (http://resolver.caltech.edu/CaltechTHESIS:11202017-145930076). https://doi.org/10.7907/Z9X06572

Roux, P. & Ben-Zion Y. (2017). Rayleigh phase velocities in Southern California from beamforming short duration ambient noise, *Geophys. J. Int.*, 211**,**450-454, doi: 10.1093/gji/ggx316.

Roy, C., & Romanowicz, B. A. (2017). On the Implications of A Priori Constraints in Transdimensional Bayesian Inversion for Continental Lithospheric Layering. *Journal of Geophysical Research: Solid Earth*, *122*(10), 10118-10131. https://doi.org/10.1002/2017JB014968

Sabra, K. G., Gerstoft, P., Roux, P., Kuperman, W. A., & Fehler, M. C. (2005). Surface wave tomography from microseisms in Southern California. *Geophysical Research Letters*, *32*(L14311), 1-4. https://doi.org/10.1029/2005GL023155

Schmandt, B., & Humphreys, E. (2010). Seismic heterogeneity and small‐scale convection in the southern California upper mantle. *Geochemistry, Geophysics, Geosystems*, *11*(5). https://doi.org/10.1029/2010GC003042

Schulte‐Pelkum, V., & Ben-Zion, Y. (2012). Apparent Vertical Moho Offsets under Continental Strike-Slip Faults from Lithology Contrasts in the Seismogenic Crust. *Bulletin of the Seismological Society of America*, *102*(6), 2757-2763. https://doi.org/10.1785/0120120139

Share, P. E., & Ben-Zion, Y. (2016). Bimaterial interfaces in the South San Andreas Fault with opposite velocity contrasts NW and SE from San Gorgonio Pass. *Geophysical Research Letters*, *43*(20), 10680-10687. https://doi.org/10.1002/2016GL070774

Shaw, J. H., & Suppe, J. (1996). Earthquake hazards of active blind‐thrust faults under the central Los Angeles basin, California. *Journal of Geophysical Research: Solid Earth*, *101*(B4), 8623-8642. https://doi.org/10.1029/95JB03453

Shaw, J. H., Plesch, A., Tape, C., Suess, M. P., Jordan, T. H., Ely, G., et al. (2015). Unified structural representation of the southern California crust and upper mantle. *Earth and Planetary Science Letters*, *415*, 1-15. https://doi.org/10.1016/j.epsl.2015.01.016

Shen, W., Ritzwoller, M. H., Schulte-Pelkum, V., & Lin, F. C. (2012). Joint inversion of surface wave dispersion and receiver functions: A Bayesian Monte-Carlo approach. *Geophysical Journal International*, *192*(2), 807–836. https://doi.org/10.1093/gji/ggs050

Shen, W., & Ritzwoller, M. H. (2016). Crustal and uppermost mantle structure beneath the United States. *Journal of Geophysical Research: Solid Earth*, *121*(6), 4306-4342. https://doi.org/10.1002/2016JB012887

Shen, Z. K., King, R. W., Agnew, D. C., Wang, M., Herring, T. A., Dong, D., & Fang, P. (2011). A unified analysis of crustal motion in Southern California, 1970–2004: The SCEC crustal motion map. *Journal of Geophysical Research: Solid Earth*, *116*(B11402), 1-19. https://doi.org/10.1029/2011JB008549

Shi, Z., & Ben-Zion, Y. (2006). Dynamic rupture on a bimaterial interface governed by slip-weakening friction. *Geophysical Journal International*, *165*(2), 469-484. https://doi.org/10.1111/j.1365-246X.2006.02853.x

Süss, M. P., & Shaw, J. H. (2003). P wave seismic velocity structure derived from sonic logs and industry reflection data in the Los Angeles basin, California. *Journal of Geophysical Research: Solid Earth*, *108*(B3). https://doi.org/10.1029/2001JB001628

Sylvester, A. G., & Smith, R. R. (1976). Tectonic transpression and basement-controlled deformation in San Andreas fault zone, Salton Trough, California. *AAPG Bulletin*, *60*(12), 2081-2102. https://doi.org/10.1306/C1EA3A73-16C9-11D7-8645000102C1865D

Taborda, R., Azizzadeh-Roodpish, S., Khoshnevis, N., & Cheng, K. (2016). Evaluation of the southern California seismic velocity models through simulation of recorded events. *Geophysical Journal International*, *205*(3), 1342-1364. https://doi.org/10.1093/gji/ggw085

Tanimoto, T., & Prindle Sheldrake, K. (2002). Three‐dimensional S‐wave velocity structure in southern California. *Geophysical research letters*, *29*(8). https://doi.org/10.1029/2001GL013486

Tanimoto, T., & Rivera, L. (2008). The ZH ratio method for long-period seismic data: sensitivity kernels and observational techniques. *Geophysical Journal International*, *172*(1), 187-198. https://doi.org/10.1111/j.1365-246X.2007.03609.x

Tape, C., Liu, Q., Maggi, A., & Tromp, J. (2009). Adjoint tomography of the southern California crust. *Science*, *325*(5943), 988-992. https://doi.org/10.1126/science.1175298

Tape, C., Liu, Q., Maggi, A., & Tromp, J. (2010). Seismic tomography of the southern California crust based on spectral-element and adjoint methods. *Geophysical Journal International*, *180*(1), 433-462. https://doi.org/10.1111/j.1365-246X.2009.04429.x

Vidale, J. E., & Helmberger, D. V. (1988). Elastic finite-difference modeling of the 1971 San Fernando, California earthquake. *Bulletin of the Seismological Society of America*, *78*(1), 122-141.

Waldhauser, F., Lippitsch, R., Kissling, E., & Ansorge, J. (2002). High-resolution teleseismic tomography of upper-mantle structure using an a priori three-dimensional crustal model. *Geophysical Journal International*, *150*(2), 403-414. https://doi.org/10.1046/j.1365-246X.2002.01690.x

Yang, Y., & Forsyth, D. W. (2006). Rayleigh wave phase velocities, small- scale convection, and azimuthal anisotropy beneath southern California. *Journal of Geophysical Research: Solid Earth*, *111*(B7). https://doi.org/10.1029/2005JB004180

Yang, Y., & Ritzwoller, M. H. (2008). Characteristics of ambient seismic noise as a source for surface wave tomography. *Geochemistry, Geophysics, Geosystems*, *9*(2). https://doi.org/10.1029/2007GC001814

Zigone, D., Ben-Zion, Y., Campillo, M., & Roux, P. (2015). Seismic tomography of the Southern California plate boundary region from noise-based Rayleigh and Love waves. *Pure and Applied Geophysics*, *172*(5), 1007-1032. https://doi.org/10.1007/s00024-014-0872-1

Table 1

Prior Distributions in Joint Inversion

Parameters	Range	Gaussian width
Sedimentary thickness	$10 \pm m_0$ (km)	0.2 km
Vsv, top of sedimentary layer	$m_0 \pm 0.5\ m_0$ (km s^{-1})	0.1 km s^{-1}
Vsv, bottom of sedimentary layer	$m_0 \pm 0.5\ m_0$ (km s^{-1})	0.1 km s^{-1}
Crust 0^{th} B-spline	$m_0 \pm 0.5\ m_0$ (km s^{-1})	0.2 km s^{-1}
Crust 2^{nd} B-spline	$m_0 \pm 0.4\ m_0$ (km s^{-1})	0.2 km s^{-1}
Crust 4^{th} B-spline	$m_0 \pm 0.4\ m_0$ (km s^{-1})	0.2 km s^{-1}
Crust 6^{th} B-spline	$m_0 \pm 0.3\ m_0$ (km s^{-1})	0.2 km s^{-1}
Crust 8^{th} B-spline	$m_0 \pm 0.2\ m_0$ (km s^{-1})	0.2 km s^{-1}

(left) A full list of the inversion parameters, (middle) the ranges explored, and (right) the gaussian half-width used to define the *a priori* distributions

Figure 1. Location map of the imaged region. Stations (blue triangles), faults (black lines), topography (grayscale), and various sub-regions are shown. Example stations FMP (yellow triangle) and WBS (red triangle) are marked, with corresponding cross-correlation H/V measurement distributions shown in Figures 2 & 4 respectively. Green and blue stars mark locations of example joint inversion results in Figures 7 and 8. Major geological features mentioned in the text are labeled in full, with the following abbreviations for major faults: San Andreas (SAF), Garlock (GF), Elsinore (EF) and San Jacinto (SJF).

Figure 2. (a) Four-component (ZR, ZZ, RR, RZ) ambient noise cross-correlations between stations FMP and WBS bandpassed around 8 s period. Clear Rayleigh waves are visible on all causal components. (b) The 8-s Rayleigh-wave particle motion in radial and vertical directions observed at receiver station WBS (left) excited by a vertical force (top) or horizontal force (bottom) at station FMP. (Right) same as (left), but with FMP being the receiver and WBS the virtual source. Stations locations are shown in Figure 1.

Figure 3. (a) H/V and (b) phase velocity sensitivity kernels for a location near San Jacinto fault (Figure 1 green star) at three different periods based on the CVMS4.26 shear-wave velocity model.

Figure 4. Distributions of H/V measurements from individual cross-correlations found from the station acting as a source (blue) or receiver (magenta) with stabilization range marked with gray dashed lines. Measurement distributions for station FMP at (a) 7 s period and (c) 15 s period. Measurement distributions for station WBS at (b) 7 s period and (d) 15 s period.

Figure 5. H/V and uncertainty maps showing individual station results (circles) and corresponding interpolation over the entire region. (a) H/V measurements at 7 seconds period. (b) H/V uncertainty, shown as the ratio of standard deviation of the mean to H/V value, for 7 s period. (c) Similar to (a) but for 15 s period. (d) Similar to (b) but for 15 s period.

Figure 6. Phase velocity and uncertainty maps. (a) Phase velocities (Vph) at 7 seconds period. (b) Vph uncertainty, shown as the ratio of standard deviation of the mean to Vph value, for 7 s period. (c) Similar to (a) but for 15 s period. (d) Similar to (b) but for 15 s period.

Figure 7. Example 1D joint inversion result at a location near the San Andreas fault (Figure 1 green star). (a) Shear wave velocity versus depth showing initial model as red triangles (CVMS), full range of model space searched (green dashes), posterior models (cyan lines), the final model (white dots), and final model standard deviation (black lines). The fixed Moho depth is also marked in gray. (b) H/V dispersion curves including H/V data (black dots), 150% of the uncertainty (error bars), predicted H/V ratios obtained from the starting model (red triangles), posterior models (cyan lines), and the final average model (white dots). (c) Similar to (b), but for phase velocities. (d) The *a priori* distribution of Vs at 0.5km depth shown in transparent histogram with thick black lines and posterior distribution in blue. The mean posterior parameter and standard deviation are shown. (e) Similar to (d) but for 2 km depth (f) Similar to (d) but for 9 km depth.

Figure 8. Same as Figure 7 but for a station in the Central Valley (Figure 1 blue star). Note the stronger gradient and shallower sediment depth in the final model (white dots) compared to the starting model (red triangles) in (a). The fit to the phase data is slightly improved (c), but the H/V fits are dramatically improved over the starting model (b).

Figure 9. Joint inversion shear velocity (Vsv, km s^{-1}) results for depth of (a) 0.5 km, (b) 2 km, and (c) 9 km. Also shown are the differences between final and starting models for depths of (d) 0.5 km (e) 2 km (f) 9 km. Cross-sections denoted in (e) are shown in Figure 11.

Figure 10. χ^2 misfit over all periods to H/V and phase velocity from the final model for (a) H/V, (b) phase velocity, and (c) joint H/V and phase velocity. Shown in (d)-(f) are results similar to (a)-(c), but from the starting model (CVMS). Note the wider scale bar for the starting compared to the final model; misfit is lower for all datasets in the final model.

Figure 11. Cross-Sections (Figure 9e) of (left) final inversion Vsv results and (right) difference between final and initial (CVMS) Vsv. (a) A-A’ cross section with the San Cayetano, San Gabriel, Clearwater, San Andreas, Lockhart and Garlock Fault surface traces marked. (b) B-B’ cross-sections with the Newport-Inglewood, Whittier, Sierra Madre and San Andreas fault surface traces marked. (c) C-C’ cross-sections with Elsinore, San Jacinto, Banning and Mill Creek fault surface traces marked. (d) D-D’ cross-section with Elsinore, San Jacinto and San Andreas fault surface traces marked. (e) E-E’ cross-section with Elsinore and Superstition Hills faults and Brawley seismic zone labeled. (f) F-F’ cross-section with San Cayetano and San Andreas faults marked. (g) G-G’ cross section with Newport-Inglewood, Sierra Madre, San Gabriel, San Andreas, and Garlock faults marked.

Figure 1.

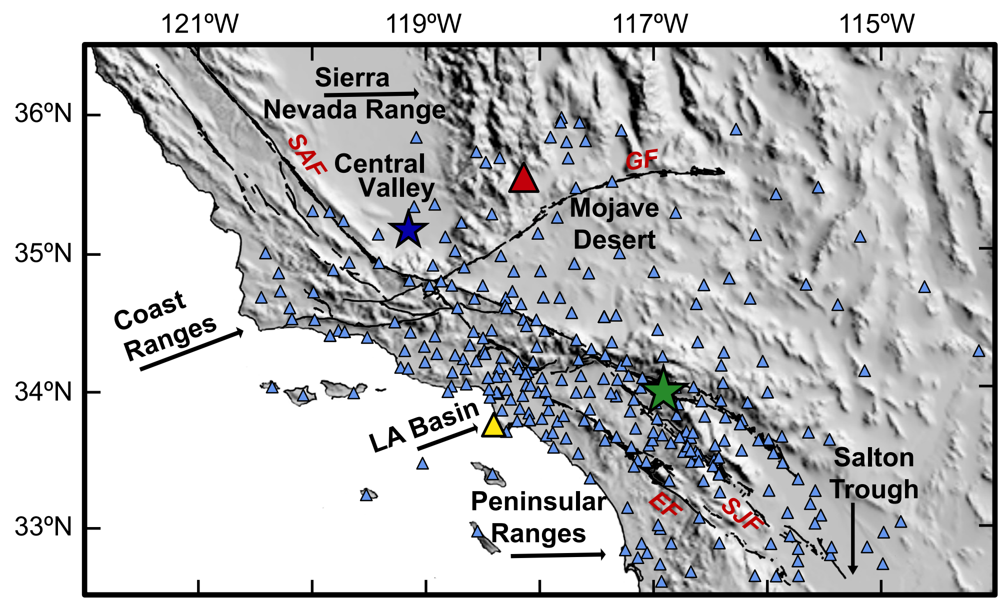

121ºW
119ºW
117ºW
115ºW
36ºN
35ºN
34ºN
33ºN
Sierra
Nevada Range
SAF
Central
Valley
GF
Mojave
Desert
Coast
Ranges
LA Basin
Peninsular
Ranges
EF
SJF
Salton
Trough

Figure 2.

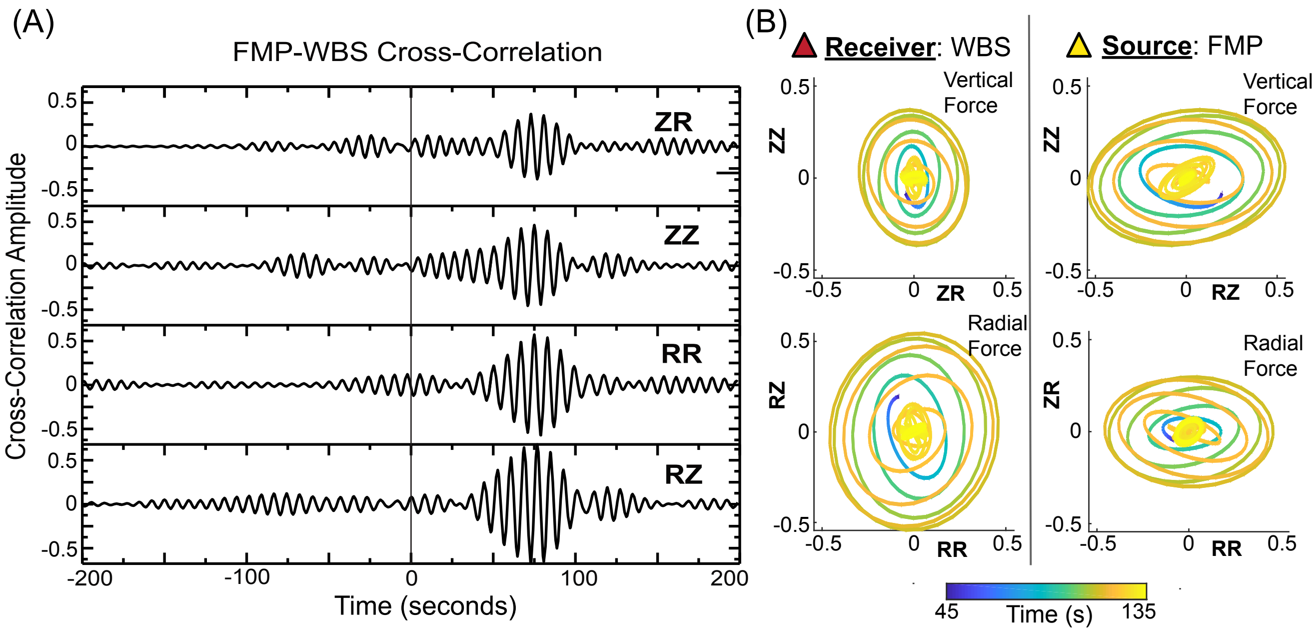

(A)
FMP-WBS Cross-Correlation
Cross-Correlation Amplitude
ZR
ZZ
RR
RZ
Time (seconds)
(B)
Receiver: WBS
Source: FMP
Vertical Force
Radial Force
Time (s)
45
135

Figure 3.

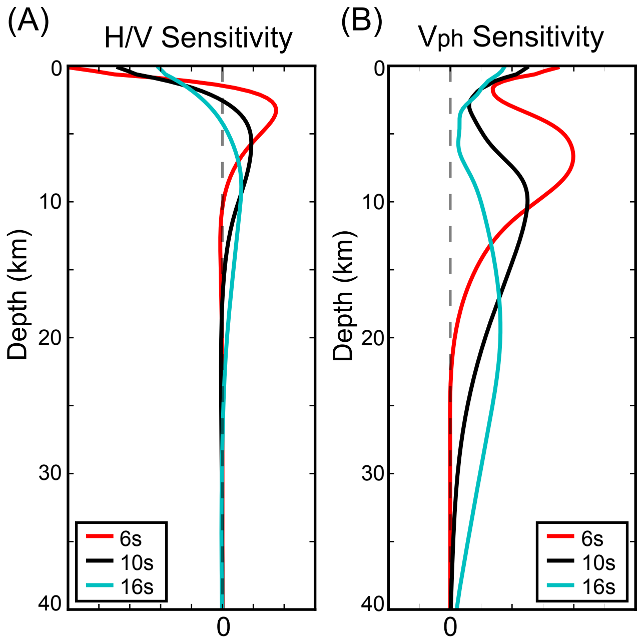

(A)
H/V Sensitivity
Depth (km)
0
10
20
30
40
0
6s
10s
16s
(B)
Vph Sensitivity
Depth (km)
0
10
20
30
40
0
6s
10s
16s

Figure 4.

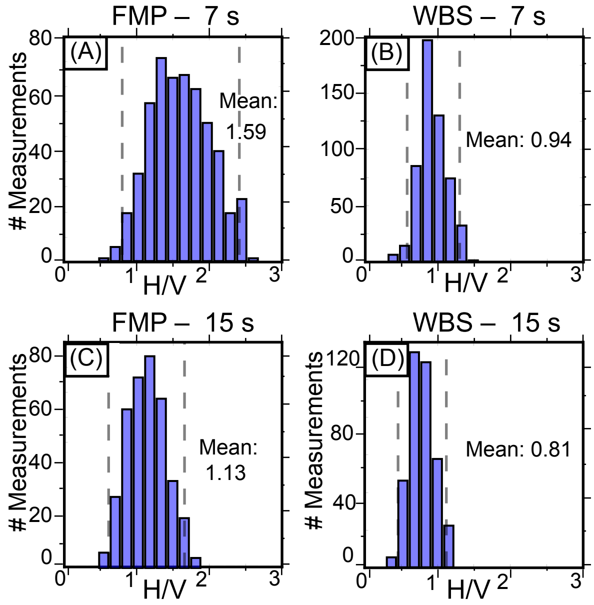
FMP – 7 s
WBS – 7 s
FMP – 15 s
WBS – 15 s
(A)
(B)
(C)
(D)
Mean: 1.59
Mean: 0.94
Mean: 1.13
Mean: 0.81
Measurements
H/V

Figure 5.

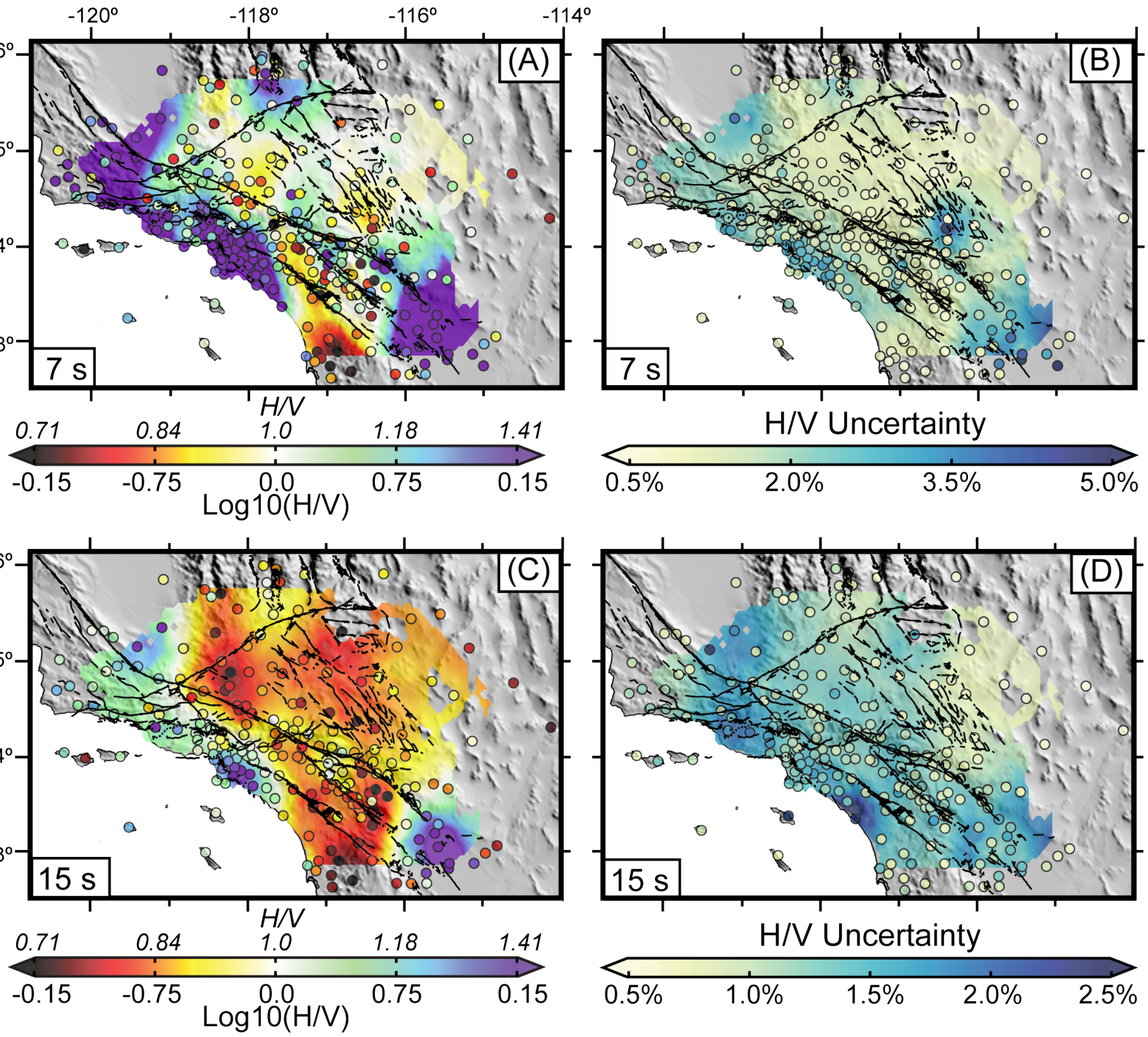

-120º
-118º
-116º
-114º
36º
35º
34º
33º
(A)
7 s
(B)
7 s
H/V
0.71
0.84
1.0
1.18
1.41
-0.15
-0.75
0.0
0.75
0.15
Log10(H/V)
H/V Uncertainty
0.5%
2.0%
3.5%
5.0%
(C)
15 s
(D)
15 s
H/V
0.71
0.84
1.0
1.18
1.41
-0.15
-0.75
0.0
0.75
0.15
Log10(H/V)
H/V Uncertainty
0.5%
1.0%
1.5%
2.0%
2.5%

Figure 6.

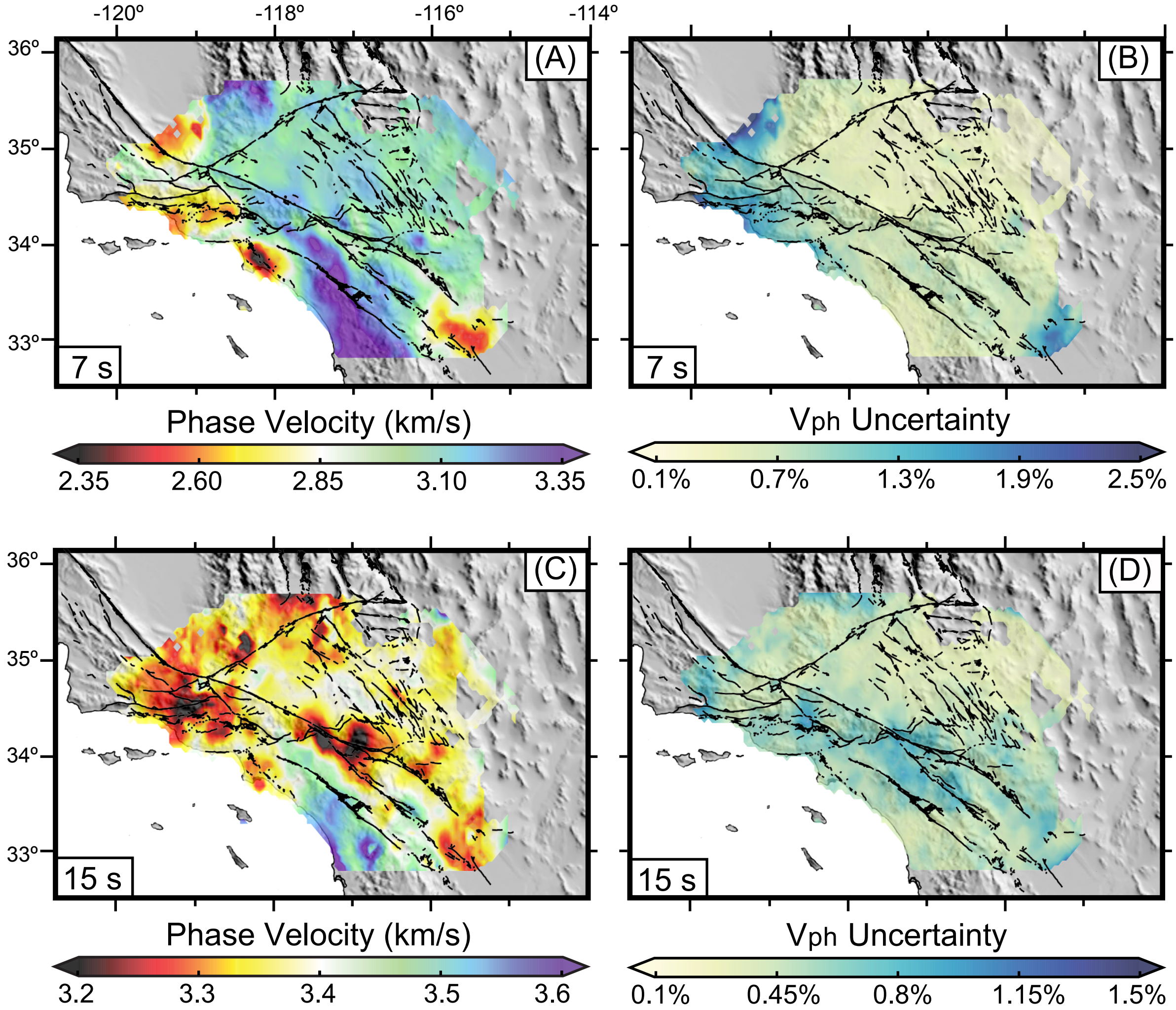

-120°
-118°
-116°
-114°
36°
35°
34°
33°
(A)
7 s
Phase Velocity (km/s)
2.35
2.60
2.85
3.10
3.35
(B)
7 s
Vph Uncertainty
0.1%
0.7%
1.3%
1.9%
2.5%
(C)
15 s
Phase Velocity (km/s)
3.2
3.3
3.4
3.5
3.6
(D)
15 s
Vph Uncertainty
0.1%
0.45%
0.8%
1.15%
1.5%

Figure 7.

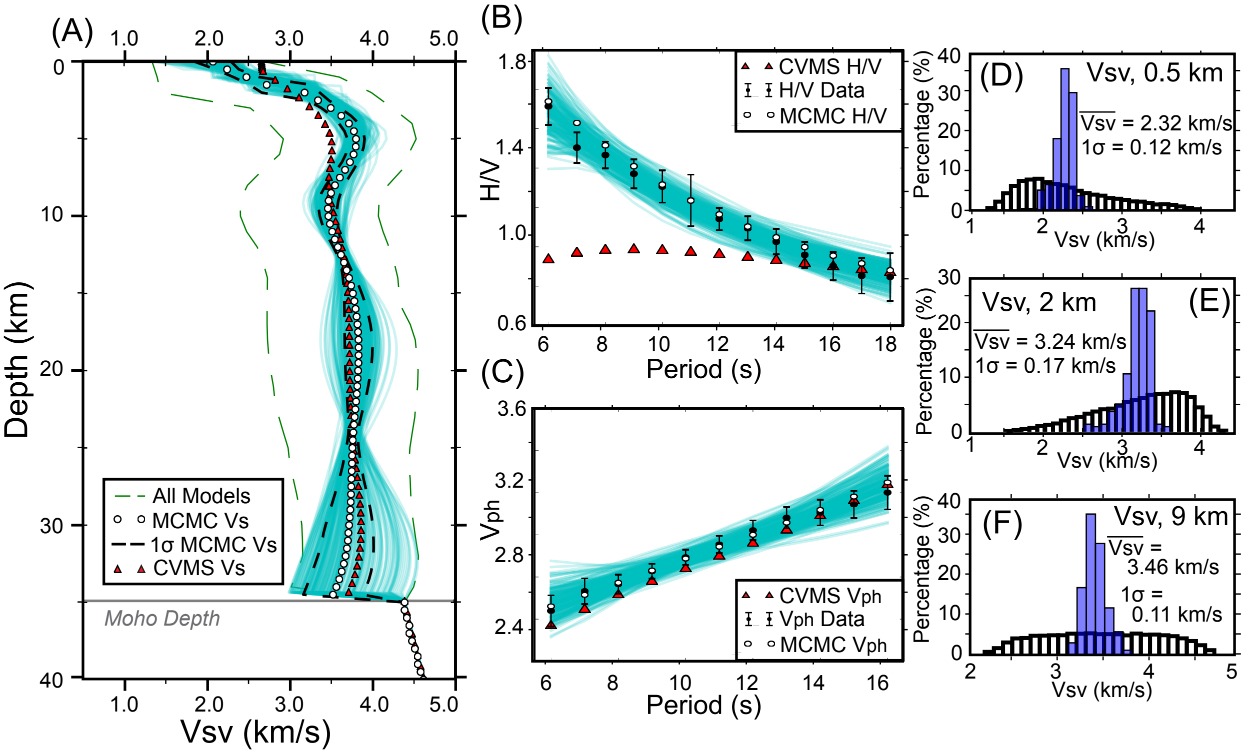

(A)
Depth (km)
Vsv (km/s)
Moho Depth
All Models
MCMC Vs
1σ MCMC Vs
CVMS Vs
(B)
H/V
Period (s)
CVMS H/V
H/V Data
MCMC H/V
(C)
Vph
Period (s)
CVMS Vph
Vph Data
MCMC Vph
(D)
Vsv, 0.5 km
Vsv = 2.32 km/s
1σ = 0.12 km/s
Percentage (%)
Vsv (km/s)
(E)
Vsv, 2 km
Vsv = 3.24 km/s
1σ = 0.17 km/s
Percentage (%)
Vsv (km/s)
(F)
Vsv, 9 km
Vsv =
3.46 km/s
1σ =
0.11 km/s
Percentage (%)
Vsv (km/s)

Figure 8.

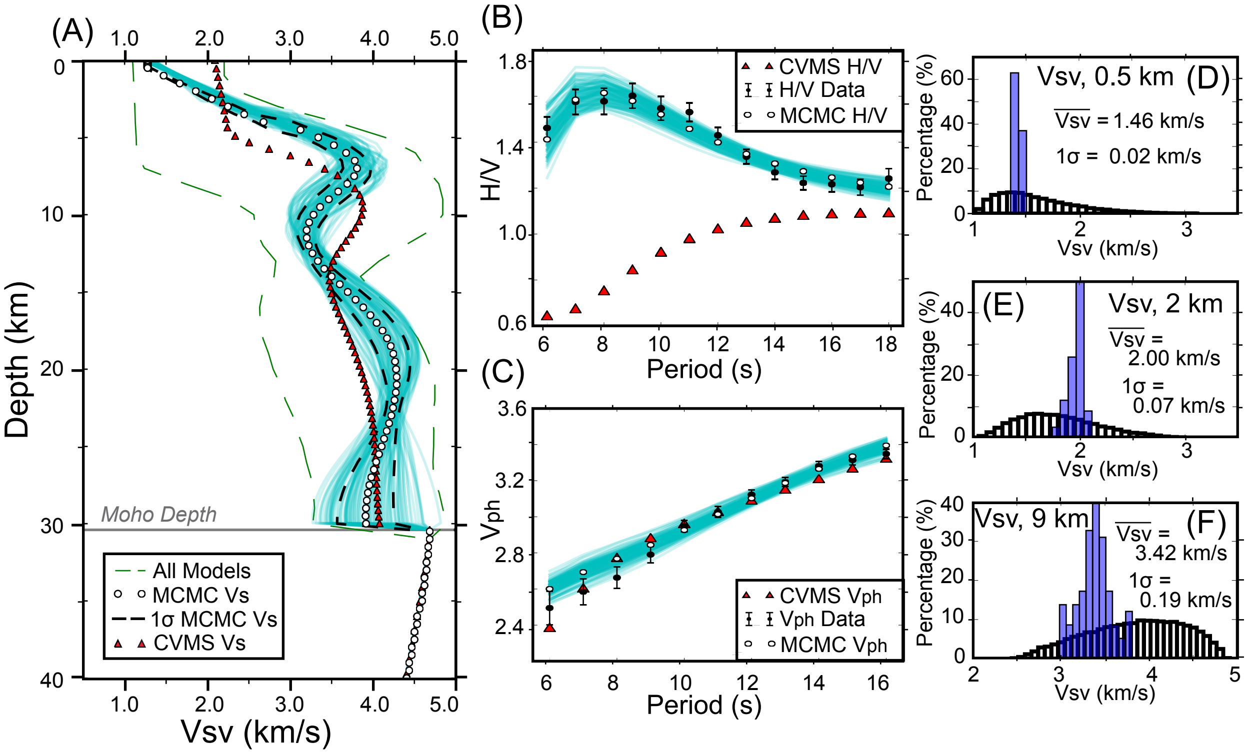

(A)
Depth (km)
Vsv (km/s)
Moho Depth
All Models
MCMC Vs
1σ MCMC Vs
CVMS Vs
(B)
H/V
Period (s)
CVMS H/V
H/V Data
MCMC H/V
(C)
Vph
Period (s)
CVMS Vph
Vph Data
MCMC Vph
Vsv, 0.5 km (D)
Vsv = 1.46 km/s
1σ = 0.02 km/s
Percentage (%)
Vsv (km/s)
(E) Vsv, 2 km
Vsv = 2.00 km/s
1σ = 0.07 km/s
Percentage (%)
Vsv (km/s)
Vsv, 9 km (F)
Vsv = 3.42 km/s
1σ = 0.19 km/s
Percentage (%)
Vsv (km/s)

Figure 9.

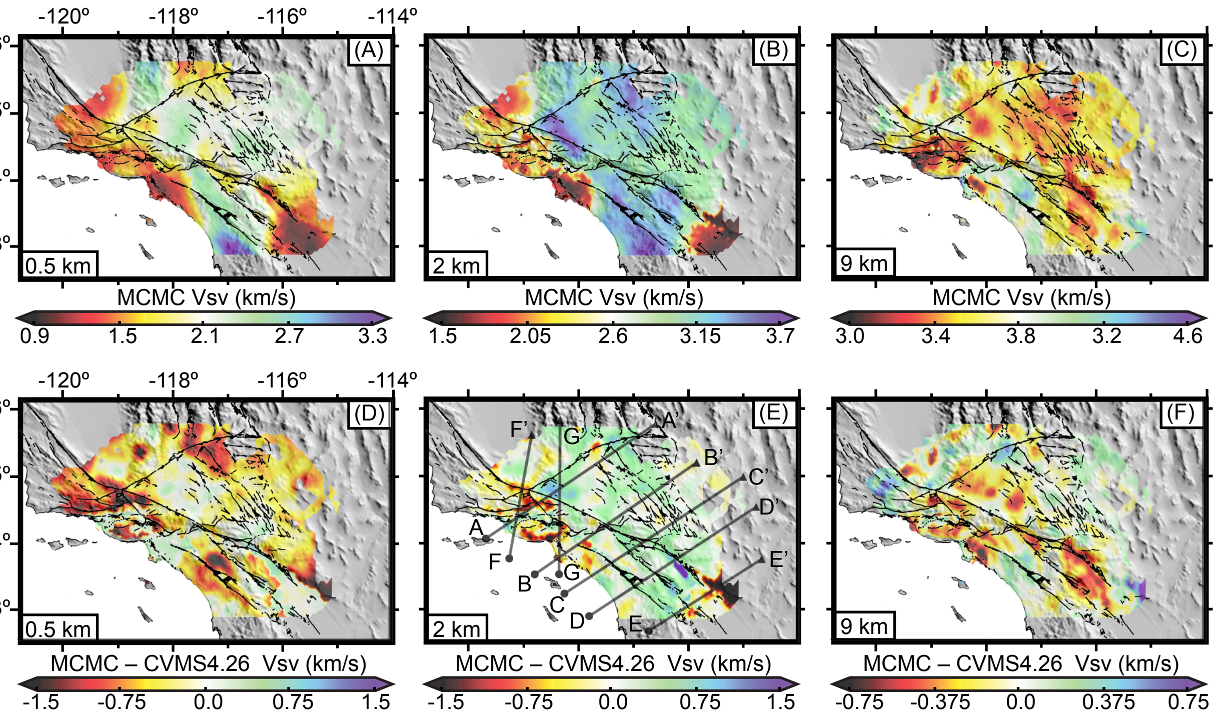
-120º
-118º
-116º
-114º
36º
35º
34º
33º
(A)
0.5 km
MCMC Vsv (km/s)
0.9
1.5
2.1
2.7
3.3
(B)
2 km
MCMC Vsv (km/s)
1.5
2.05
2.6
3.15
3.7
(C)
9 km
MCMC Vsv (km/s)
3.0
3.4
3.8
3.2
4.6
(D)
0.5 km
MCMC – CVMS4.26 Vsv (km/s)
-1.5
-0.75
0.0
0.75
1.5
(E)
A
A'
B
B'
C
C'
D
D'
E
E'
F
F'
G
G'
2 km
MCMC – CVMS4.26 Vsv (km/s)
-1.5
-0.75
0.0
0.75
1.5
(F)
9 km
MCMC – CVMS4.26 Vsv (km/s)
-0.75
-0.375
0.0
0.375
0.75

Figure 10.

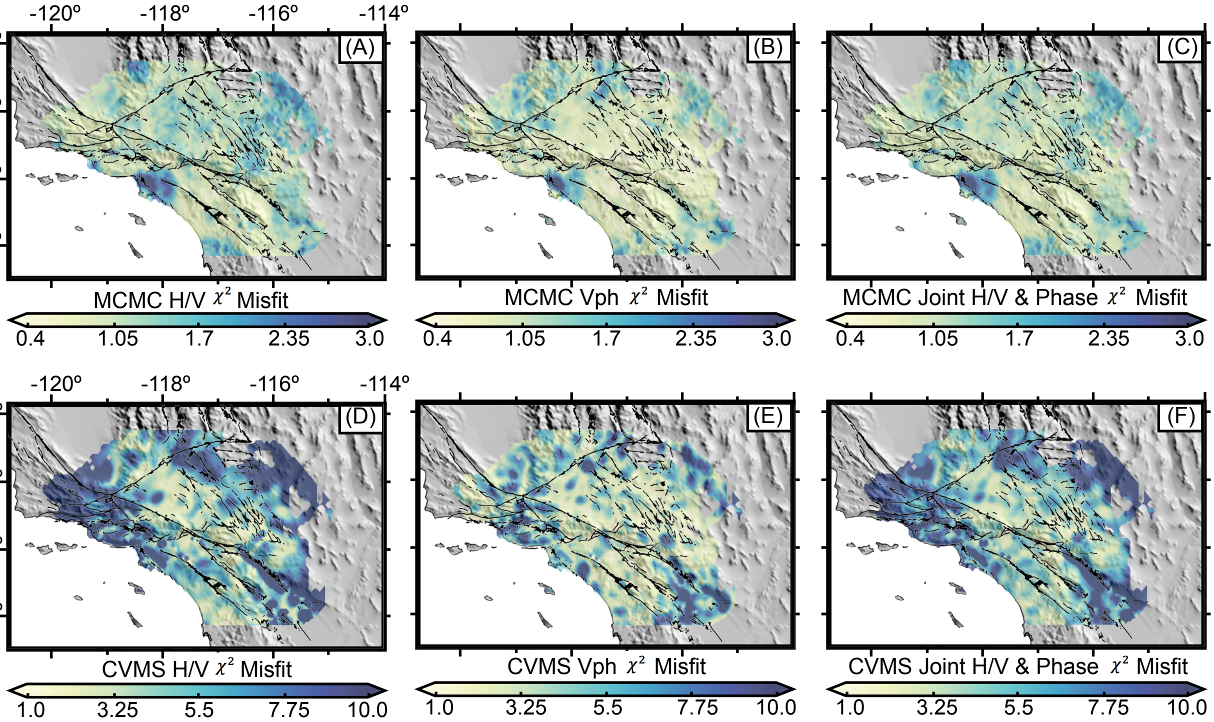

-120º
-118º
-116º
-114º
36º
35º
34º
33º
(A)
MCMC H/V χ² Misfit
0.4
1.05
1.7
2.35
3.0
(B)
MCMC Vph χ² Misfit
0.4
1.05
1.7
2.35
3.0
(C)
MCMC Joint H/V & Phase χ² Misfit
0.4
1.05
1.7
2.35
3.0
-120º
-118º
-116º
-114º
36º
35º
34º
33º
(D)
CVMS H/V χ² Misfit
1.0
3.25
5.5
7.75
10.0
(E)
CVMS Vph χ² Misfit
1.0
3.25
5.5
7.75
10.0
(F)
CVMS Joint H/V & Phase χ² Misfit
1.0
3.25
5.5
7.75
10.0

Figure 11.

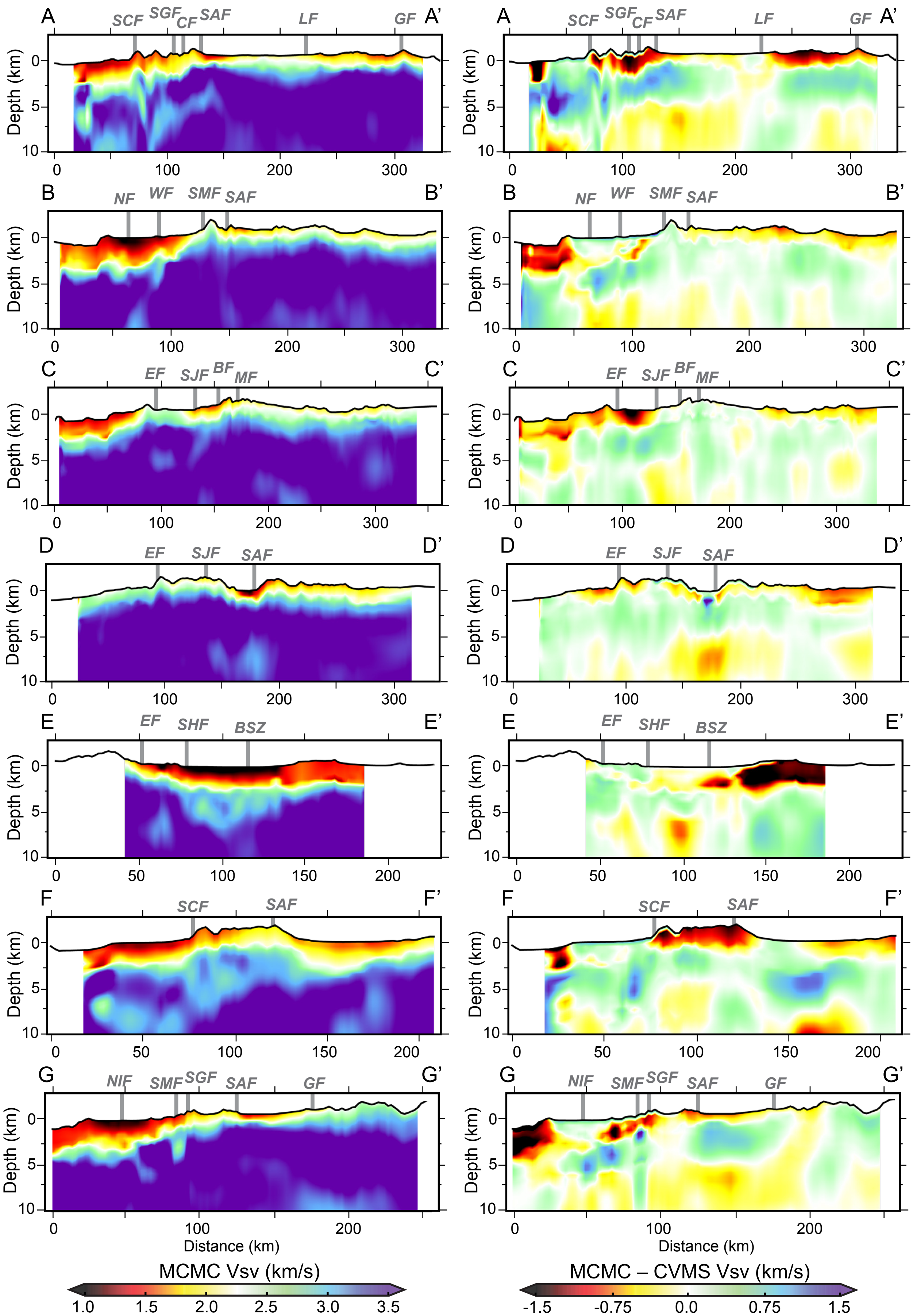

A
A'
SCF
SGF
CF
SAF
LF
GF
B
B'
NF
WF
SMF
C
C'
EF
SJF
BF
MF
D
D'
E
E'
SHF
BSZ
F
F'
G
G'
NIF
Depth (km)
Distance (km)
MCMC Vsv (km/s)
1.0
1.5
2.0
2.5
3.0
3.5
MCMC – CVMS Vsv (km/s)
-1.5
-0.75
0.0
0.75
1.5